Isolated Metal Active Site Concentration and Stability Control Catalytic CO$_2$ Reduction Selectivity

John C. Matsubu,[†] Vanessa N. Yang,[†] and Phillip Christopher*,[†,‡]

[†]Department of Chemical & Environmental Engineering, and [‡]Program in Materials Science and Engineering, University of California, Riverside, Riverside, California 92521, United States

S *Supporting Information*

ABSTRACT: CO$_2$ reduction by H$_2$ on heterogeneous catalysts is an important class of reactions that has been studied for decades. However, atomic scale details of structure−function relationships are still poorly understood. Particularly, it has been suggested that metal particle size plays a unique role in controlling the stability of CO$_2$ hydrogenation catalysts and the distribution of active sites, which dictates reactivity and selectivity. These studies often have not considered the possible role of isolated metal active sites in the observed dependences. Here, we utilize probe molecule diffuse reflectance infrared Fourier transform spectroscopy (DRIFTS) with known site-specific extinction coefficients to quantify the fraction of Rh sites residing as atomically dispersed isolated sites (Rh$_{iso}$), as well as Rh sites on the surface of Rh nanoparticles (Rh$_{NP}$) for a series of TiO$_2$ supported Rh catalysts. Strong correlations were observed between the catalytic reverse water gas shift turn over frequency (TOF) and the fraction of Rh$_{iso}$ sites and between catalytic methanation TOF and the fraction of Rh$_{NP}$ sites. Furthermore, it was observed that reaction condition-induced disintegration of Rh nanoparticles, forming Rh$_{iso}$ active sites, controls the changing reactivity with time on stream. This work demonstrates that isolated atoms and nanoparticles of the same metal on the same support can exhibit uniquely different catalytic selectivity in competing parallel reaction pathways and that disintegration of nanoparticles under reaction conditions can play a significant role in controlling stability.
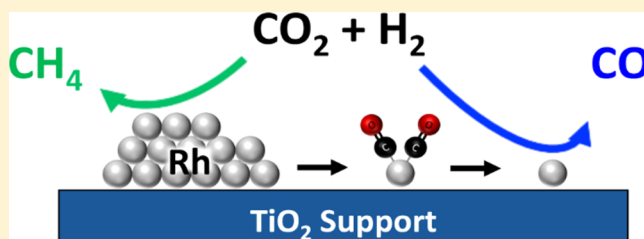
1. INTRODUCTION

Approaches for designing optimal heterogeneous catalysts rely on structure−function relationships between active site characteristics and performance. Variations in metal surface structure on model single crystal catalysts, or in size- and shape-controlled metal nanoparticles, have often been exploited to experimentally correlate active site geometries to catalytic reactivity.[1−6] However, it has been identified that isolated metal atoms on oxide supports can play an unexpected role in governing the reactivity of heterogeneous metal catalysts, and that metallic nanostructures can undergo significant geometric changes under reaction conditions.[7−13] These findings raise questions as to the validity of surface structure-based active site identification strategies.

Inconsistencies in catalytic structure−function relations have recently been highlighted in efforts dedicated to designing catalysts for the selective reduction of CO$_2$ by H$_2$ to produce higher valued products. Studies examining reactivity and selectivity trends for CO$_2$ reduction by H$_2$ over heterogeneous transition metal catalysts have hypothesized that particle size is a dominant characteristic controlling catalyst performance and stability under reaction conditions.[5,14−18] However, transmission electron microscopy (TEM)-based studies have qualitatively suggested that isolated transition metal sites may also contribute to metal weight loading-dependent selectivity and stability trends.[19,20] Direct evidence relating hypothesized particle size and isolated site-dependent phenomena in CO$_2$ reduction catalysis to the nature of active sites controlling catalytic functionality is lacking.

Herein, we show quantitative evidence that isolated Rh sites on TiO$_2$ supports are responsible for controlling catalytic selectivity and stability in CO$_2$ reduction by H$_2$. Using probe molecule infrared spectroscopy, the fraction of catalytically active Rh sites existing as atomically dispersed isolated sites (Rh$_{iso}$) and as Rh sites on the surface of Rh nanoparticles (Rh$_{NP}$) was quantified for a series of catalysts. Strong correlations were observed between the catalytic reverse water gas shift (r-WGS, CO$_2$ + H$_2$ ←→ CO + H$_2$O) turn over frequency (TOF) and the fraction of Rh$_{iso}$ sites and between catalytic methanation (CO$_2$ + 4H$_2$ ←→ CH$_4$ + 2H$_2$O) TOF and the fraction of Rh$_{NP}$ sites. Further, it was found that Rh nanoparticle disintegration under reaction conditions to form Rh$_{iso}$ sites controls the instability of catalytic selectivity. Our work highlights stark differences in selectivity exhibited by atomically dispersed and nanoparticle-based active catalytic sites in parallel reaction pathways and that interconversion between these site types is a dynamic process under reaction conditions, providing important information for the design of selective CO$_2$ reduction catalysts.

2. EXPERIMENTAL METHODS

2.1. Materials. Catalyst precursor rhodium nitrate hydrate $(Rh(NO_3)_3 \cdot xH_2O)$ (~36% Rh) was purchased from Sigma-Aldrich. TiO_2 nanoparticle support (P25) was obtained from Evonik. 35% hydrogen peroxide (H_2O_2) and 37% hydrochloric acid (HCl) were both obtained from Fisher Scientific. All gases used in synthesis, characterizations, and reactions were purchased from Airgas, with the purities and concentrations mentioned in their respective sections.

2.2. Material Synthesis. Five weight loadings of Rh (0.5%, 2%, 3%, 4%, and 6%) were deposited on TiO_2 nanoparticles (Evonik P25), to produce total sample masses of 300 mg each, using a simple impregnation technique. The quantity of $(Rh(NO_3)_3 \cdot xH_2O)$ necessary for each weight loading was dissolved in an evaporation dish with 600 μL of water. TiO_2 was mixed with the aqueous Rh solution using a stir rod until homogeneous in appearance, dried at 95 °C for 4 h, ground up with a mortar and pestle, and calcined in a tube furnace at 450 °C in air for 4 h. In situ reduction of the catalysts in pure H_2 (99.999%) at 350 °C for 1 h was performed to obtain the desired metallic Rh oxidation state prior to CO chemisorption-based analyses (volumetric and diffuse reflectance infrared Fourier transform spectroscopy (DRIFTS)), reactivity experiments in the packed bed reactors, and the leaching treatment. A leaching procedure was developed to selectively dissolve Rh nanoparticles off the TiO_2 surface without removing isolated Rh atoms from the TiO_2 surface.[21] The leaching process was executed by suspending 100 mg of reduced catalyst in 10 mL of 11.6 M HCl/1% H_2O_2 solution while constantly stirring for 3 h at 65 °C. The sample was then washed four times in distilled water, separated using centrifugation, dried at 95 °C for 4 h, and reduced in situ prior to catalytic testing or DRIFTS analysis.

2.3. Characterization Techniques. *2.3.1. Transmission Electron Microscopy.* Reduced samples were characterized using a Philips CM300 transmission electron microscope (TEM) operated at 300 kV accelerating voltage. After reduction, sample powders were suspended in distilled water using ultrasonication and added dropwise onto a holey carbon-coated copper grid sample holder. Rh particle size distributions were determined by measuring the diameter of at least 100 particles for each sample via ImageJ software.

2.3.2. Volumetric CO Chemisorption. Volumetric CO chemisorption analyses were performed with a Micromeritics ASAP 2020. Catalysts were packed in a quartz tube sample holder and heated in H_2 at a heating rate of 10 °C/min to 350 °C with a reduction time at 350 °C of 1 h. The sample was evacuated at 350 °C for 10 min and cooled to 35 °C under vacuum prior to CO chemisorption analysis. Two CO adsorption isotherms were performed (at 35 °C and from 100 to 450 mmHg) with an evacuation step between the two to remove physisorbed CO. The first isotherm represented both irreversible-chemisorption and reversible-physisorption, where the second isotherm only involved the reversible-physisorption. The difference between the two isotherms represented the total amount of CO chemisorbed to surface Rh atoms. An assumed ratio of 1 CO molecule per surface Rh atom was used to convert the number of chemisorbed CO molecules into the number of surface Rh atoms. This value was corrected, as described below, to account for CO adsorption geometries with non 1:1 CO:Rh ratios.

2.3.3. DRIFTS CO Chemisorption. Catalyst samples were packed into a Harrick Praying Mantis high temperature reaction chamber (ZnSe windows) mounted inside of a Thermo Scientific Praying Mantis diffuse reflectance adapter, set inside of a Thermo Scientific Nicolet iS10 FT-IR spectrometer. Gases were flowed to the reaction chamber using Teledyne mass flow controllers. This setup was used to quantitatively determine the fraction of Rh_{iso} and Rh_{NP} sites on each catalyst. In all measurements, spectra were obtained by averaging 40 sequentially collected scans at a resolution of 4 cm^{-1}. The spectra were obtained in Kubelka–Munk (KM) units, which have been shown to scale linearly with adsorbate concentration.[22] This analysis was used in three different applications: quantifying the Rh_{iso} and Rh_{NP} site fractions of freshly prepared reduced catalysts, quantifying the impact of reaction conditions on the relative quantity of site type fractions, and verifying that the CO chemisorption analyses did not significantly

alter the site fractions or structure of the samples during the process of characterization.

Site Fraction Quantification. Approximately 30 mg of pure TiO_2 (Evonik P25) was packed in the reaction chamber (to minimize use of the Rh/TiO_2 samples), and approximately 10 mg of each Rh/TiO_2 sample was then packed on top. For the 4% and 6% Rh weight loading samples, a 1:1 dilution of the top 10 mg of Rh loaded samples with plain TiO_2 was used to improve the signal by reducing absorption. The samples were purged with pure H_2 (99.999%) at 100 sccm for 15 min at room temperature and then reduced in pure H_2 at 20 sccm and 350 °C for 1 h. The reactor was then cooled to room temperature and purged with Ar (99.999%) at 100 sccm for 10 min, and then a baseline spectrum was taken of the sample. 50 sccm of a 10% CO/90% Ar stream was then introduced to the sample for 10 min to allow for complete CO adsorption. The sample was then purged with 100 sccm Ar for 10 min, and a DRIFT spectrum was acquired to quantitatively determine the fraction of both Rh_{iso} and Rh_{NP} sites. To verify that 10 min of CO adsorption was enough time to reach monolayer saturation and examine the stability of the catalysts during the site fraction quantification, the site fractions were also monitored on a per minute basis during the CO exposure and Ar purge steps. The peak intensities, I_i, were determined from deconvolution using Omnic software and were converted into site fractions using previously determined extinction coefficients[23] for each vibrational mode and the following equation:

$$X_{iso} = \frac{I_{iso}/\left(\varepsilon_{iso} \times \left(\frac{CO}{Rh}\right)_{iso}\right)}{\sum_{i=1}^{3}\left[I_i/\left(\varepsilon_i \times \left(\frac{CO}{Rh}\right)_i\right)\right]} \tag{1}$$

The three types of CO configurations considered were *gem*-dicarbonyl (Rh_{iso}), linear (Rh_{NP}), and bridge bound (Rh_{NP}), where the Rh_{iso} sites were quantified on the basis of the intensity of the symmetric *gem*-dicarbonyl CO stretch. Rh_{NP} site fraction (X_{NP}) was calculated as $X_{NP} = 1 - X_{iso}$. The extinction coefficients, ε_i, used for the symmetric *gem*-dicarbonyl, linear, and bridge configurations were 74, 26, and 85 $(cm/mol)(10^8)$, respectively.[23] The extinction coefficients were used from an earlier study on Rh/Al_2O_3, where the nature of the support may slightly affect the extinction coefficient, particularly the *gem*-dicarbonyl species, although the similarity of vibrational frequencies of the *gem*-dicarbonyl species on the two supports suggests that this difference would not impact our results. The CO:Rh ratios for the symmetric *gem*-dicarbonyl, linear, and bridge configurations were 2, 1, and 0.5, respectively.

Volumetric CO Chemisorption Mimic Experiment. To examine catalyst stability during the volumetric CO chemisorption measurements (section 2.3.2), we designed a DRIFTS-based experiment to mimic the volumetric measurements while simultaneously quantifying Rh_{iso} and Rh_{NP} site fractions. The experiment utilized the same procedure described above to determine the initial site fractions and utilized flowing 10% CO/Ar and Ar (99.999%) over the sample to mimic the CO adsorption isotherm and evacuation steps, respectively. After the initial site fractions were measured, the 6% Rh/TiO_2 sample was heated from 25 to 35 °C and exposed to 10% CO/Ar flow for 3 h, followed by pure Ar flow for 1 h and finally 3 h with flowing 10% CO/Ar while simultaneously collecting DRIFT spectra every 10 min. Spectra processing and site quantification was executed identically to the approach described above.

Reaction Conditions Induced Catalyst Restructuring. To study the effect of reaction conditions on the Rh_{NP} and Rh_{iso} site fractions, the same procedure as mentioned above was performed to obtain initial site fractions, followed by 90 min under reaction conditions and then post reaction CO adsorption analysis. All of these steps were performed sequentially, in situ, in the Harrick reaction chamber. After the initial CO adsorption spectrum was acquired, the reactor was purged and heated to a reaction temperature of 200 °C under 100 sccm Ar flow. All five Rh weight loadings were tested at the 10CO_2:H_2 ratio to mimic the reaction conditions explored in the catalytic testing experiments. After 90 min at reaction conditions, the samples were

purged with Ar and cooled back to 25 °C where a new background was obtained. CO adsorption, followed by Ar purging and DRIFT spectra collection, was then executed on the postreaction samples. The CO DRIFT spectra were processed in the same manner described above to determine how and to what degree the site fractions changed as a function of Rh weight loading due to reaction conditions.

2.4. Reactor Experiments. Catalysts were reduced in situ at 350 °C for 1 h in pure H_2 prior to catalytic testing. All CO_2 reduction reaction rates were measured using 15−30 mg of catalyst at 200 °C in a 1/4″ OD borosilicate packed bed reactor operating at atmospheric pressure and running under differential reactor conditions (conversion of limiting reagent <10%) with the effluent quantified by online gas chromatography (SRI MG #3). CO_2 was separated from other gases using a Hayesep D column, while H_2, N_2, CH_4, and CO were separated using a molecular sieve (MS13X) packed column. The separated gases were then quantified using a helium ionization detector (HID) and a thermal conductivity detector (TCD). The total reactant flow rate in all studies was 100 standard cm^3 per minute (sccm). Gases were delivered via Teledyne mass flow controllers. The $CO_2:H_2$ ratio was varied from stoichiometric methanation conditions, 1:4, to H_2-lean conditions, 10:1, by varying individual flow rates. Inert N_2 carrier gas was used at all conditions with a flow rate of greater than 89 sccm. It is important to note that for each reaction condition a fresh sample was loaded into the reactor to ensure each experiment was measuring the reactivity of freshly prepared samples. Reaction rates and selectivity were calculated on the basis of the average of five measurements taken during the first hour on stream. See Supporting Information Table S1 for experimental details regarding reactant flow rates for each condition.

2.5. TOF Calculations. In this work, we will report overall TOFs on the basis of reaction rates per total number of sites (Rh_{iso} + Rh_{NP}) and site-specific TOFs, which refer to the TOFs for a specific reaction on the basis of specific site type concentration (Rh_{iso} or Rh_{NP}). Below we will describe our approach to calculating overall TOFs, and the site-specific TOF calculation is discussed in the Results. Hereafter, site-specific TOFs will be denoted as so, and all other mentions of TOF will be on an overall sites basis. CO can adsorb to Rh sites in three main configurations, the *gem*-dicarbonyl, linear, and bridge configurations, which exhibit CO to Rh ratios (CO:Rh) of 2:1, 1:1, and 1:2, respectively. Different fractions of each site type exist for each Rh weight loading, and thus the overall CO:Rh ratios will be different for each weight loading when a saturated CO monolayer is added. Therefore, the ratio of 1:1 for CO:Rh assumed in the volumetric CO chemisorption analysis must be corrected to account for the varying CO:Rh ratio and allow for accurate TOF calculations in the units molecules/Rh atom/s for each catalyst. The correct ratio of CO:Rh was determined from the DRIFTS analysis described above by determining the fraction of each CO adsorption site type for each Rh weight loading. Finally, the number of Rh sites per weight of catalyst measured by volumetric CO chemisorption was divided by the CO:Rh ratio measured in the DRIFTS experiments to provide an accurate Rh site concentration for each catalyst weight loading, which was used in the TOF calculations.

3. RESULTS

3.1. Site-Specific Reactivity. The five weight loadings of Rh on TiO_2 were characterized by TEM and DRIFTS CO chemisorption to determine Rh nanoparticle sizes and the fraction of Rh sites existing as Rh_{NP} and Rh_{iso}. Representative micrographs of each Rh weight loading and the measured average particle sizes are shown in Supporting Information Figure S1. Only small variations in average particle sizes were observed, ranging from 1 to 1.5 nm for Rh weight loadings 0.5−4% (all within measurement error) and increasing to 2.5 nm for the 6% Rh weight loading. It is important to note that we made no attempt to quantify isolated site concentration from TEM, due to the difficulty of detecting the species and the very small sample size we would obtain in such a measurement,

and thus the reported particle size represents the average size of metallic particles with diameter greater than ~0.3 nm.

Figure 1a shows a typical DRIFT spectrum acquired following CO adsorption at 300 K on a fresh, reduced 4%
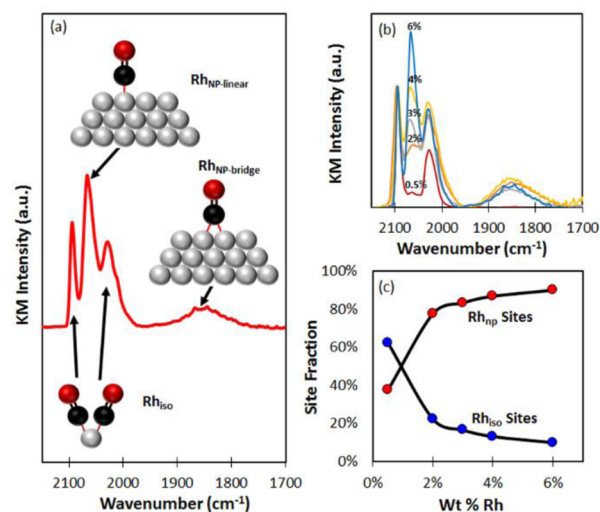
Figure 1. (a) DRIFT spectrum obtained from a saturated layer of CO adsorbed at 300 K on 4% Rh/TiO_2. Insets show ball-and-stick models of assigned vibrational modes. (b) DRIFT spectra of CO on all five weight loadings of Rh/TiO_2 catalysts. The spectra are displayed in Kubelka−Munk (KM) units and normalized by the symmetric *gem*-dicarbonyl peak (2097 cm^{-1}) height to allow for comparison. (c) Site fraction (%) of isolated (Rh_{iso}) and nanoparticle-based Rh sites (Rh_{NP}), calculated on the basis of eq 1 and the spectra in (b), as a function of wt % Rh.

Rh/TiO_2 catalyst. The peaks at ~2097 and ~2028 cm^{-1} are associated with the symmetric and asymmetric stretches of the Rh(CO)$_2$ *gem*-dicarbonyl species that exist uniquely at Rh_{iso} sites on the TiO_2 support.[24,25] The assignment of these peaks to an isolated Rh atom on a support with two CO molecules bound to it has been thoroughly substantiated in previous studies.[23−26] The peaks at 2068 and 1860 cm^{-1} are associated with CO adsorbed in linear and bridge bound geometries at Rh_{NP} sites.[24,25] Schematic depictions of these adsorption geometries are shown in Figure 1a. The DRIFT spectra obtained for CO on all five Rh weight loadings are shown in Figure 1b and normalized by the symmetric *gem*-dicarbonyl peak height. Variations in the linear CO peak height with Rh weight % correlate to increasing fractions of Rh_{iso} sites. A similar trend was not observed for the bridge bound CO geometry. This inconsistency was due to the broader and weaker nature of this peak along with it residing between the asymmetric *gem*-dicarbonyl and adsorbed water peaks at lower wavenumber (not shown here), which made this species consistently difficult to baseline and quantify. The absolute intensity of the bridge peak had a minimal impact on the quantified Rh_{NP} and Rh_{iso} site fractions, due to its low magnitude and high extinction coefficient. The fractions of each site type (Rh_{iso} and Rh_{NP}) were quantified for the five catalyst weight loadings, using eq 1 and the spectra in Figure 1b, and are shown in Figure 1c.[23] At the smallest Rh weight loading (0.5%), a relatively high fraction of Rh_{iso} sites exists on the TiO_2 support (~62%), Figure 1c. The fraction of Rh_{iso} sites drops significantly (<20%) as the Rh weight loading was increased to 2%. Our results are consistent with prior literature,[26]

demonstrating that the CO:Rh ratio in a saturated CO monolayer decreased with increasing Rh weight % loading. We observed that the CO:Rh ratios at saturation coverage were 1.62, 1.13, 1.12, 1.04, and 1.06 for the 0.5%, 2%, 3%, 4%, and 6% Rh catalysts, respectively. Alternative to site fraction, Supporting Information Figure S2 shows the concentration (number of sites per gram catalyst) of Rh_{iso} and Rh_{NP} site types as a function of Rh weight % loading. The concentration of Rh_{NP} sites increased ~5-fold as Rh wt % increased from 0.5% to 2% and remained constant from 2% to 6%, whereas the concentration of Rh_{iso} sites gradually decreased as Rh wt % increased from 0.5% to 6%.

It is well-known that CO can induce restructuring of supported Rh nanostructures, even at ambient conditions[27] similar to those used in our DRIFTS and volumetric CO chemisorption analyses of site fractions and total site concentration.[26] We performed experiments to monitor site fractions over time during the course of these analyses to ensure that the measurements themselves were not inducing changes in catalyst structure or site fraction. As shown in Supporting Information Figure S3, the site fractions were relatively constant during the course of the DRIFTS CO chemisorption studies, exhibiting only a small change toward the end of the 10 min Ar purge after CO adsorption. The reasonable stability during the first 15 min of the experimental protocol used in these measurements justifies that the site fractions in Figure 1c are good representations of the freshly synthesized and reduced catalysts. Another experiment was performed to verify the experimental procedure for volumetric CO chemisorption measurements did not impact the site fractions. We mimicked the volumetric measurements in situ in the DRIFTS reaction cell and observed constant site fractions during the course of the experiment, Supporting Information Figure S4. These two experiments justify that the site fraction and Rh:CO values derived from the DRIFTS and volumetric CO chemisorption measurements (that are used for TOF calculations) are an excellent representation of the fresh synthesized and reduced catalysts. To summarize the catalyst characterization, it was seen while the relative site fractions of Rh_{iso} and Rh_{NP} vary most significantly for the smaller weight loading catalysts (0.5–3% Rh), the particle size was constant for all weight loadings except the highest (6% Rh).

Catalytic selectivity toward CH_4 production (r-WGS, CO production, is the competing reaction) was measured for the five Rh weight loadings on TiO_2 under varying $CO_2:H_2$ ratios, Figure 2. Under stoichiometric methanation conditions ($CO_2:4H_2$), 0.5% Rh/TiO_2 exhibited a CH_4 selectivity of 65%, whereas all other weight loadings exhibited >98% CH_4 selectivity. As the $CO_2:H_2$ ratio was increased to more CO_2-rich conditions, the CH_4 selectivity decreased at all weight loadings, which is consistent with the positive CO_2 reaction order for r-WGS and zero reaction order for methanation over Rh catalysts.[28] For all $CO_2:H_2$ feed ratios tested, a positive dependence of CH_4 selectivity on Rh weight loading was observed. It is important to note that the effect of H_2 conversion on selectivity was considered in Supporting Information Figure S5, and the high selectivity across the whole range of conversions suggests conversion is not the primary driver for the trends observed, as expected on the basis of the low conversions. By examining the CO and CH_4 production TOFs separately, as a function of Rh weight loading as shown in Figure 3 and Supporting Information
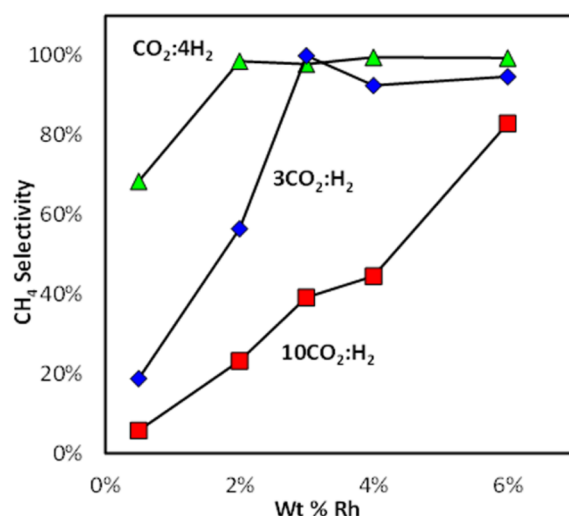
Figure 2. CH_4 selectivity as a function of wt % Rh for 0.25, 3, and 10 $CO_2:H_2$ feed ratios measured at 200 °C.

Figure S6, respectively, we can explore the origin of the CO_2 reduction selectivity dependence on Rh weight loading.

Figure 3a–c shows an agreement between the trend of CO production TOF and fraction of Rh_{iso} sites as a function of Rh weight loading for the three conditions tested. In this plot, the site concentration and reaction rates are both normalized on a per total Rh sites basis, providing site fraction and TOF, respectively, allowing a consistent comparison. Of particular note is that the relative magnitude of change of the CO production TOFs and Rh_{iso} site fractions as a function of Rh weight loading are quantitatively similar. For example, at 3:1 $CO_2:H_2$ feed ratio, the CO production TOF decreased from 0.57×10^{-3} to 0.29×10^{-3} CO molecules/Rh atom/s as the weight loading was increased from 0.5% to 2% Rh, where a similar ~3-old decrease in Rh_{iso} site fraction was observed. A similar consistency is seen between the Rh weight loading-dependent CH_4 production TOF and the fraction of Rh_{NP} sites in Supporting Information Figure S6.

The trend between CO production TOF and Rh_{iso} site fraction was evaluated through an alternative comparison by plotting the rate of r-WGS per gram catalyst as a function of number of Rh_{iso} sites per gram catalyst, as shown in Supporting Information Figure S7. Linearity in the plot for each $CO_2:H_2$ feed ratio corresponds to the agreement between Rh_{iso} site fraction and r-WGS TOF shown in Figure 3. The slopes of the lines in Supporting Information Figure S7 provide site-specific TOF for r-WGS exclusively on Rh_{iso} sites and are an average of the site-specific TOF measured across all tested catalysts at a given condition. For example, the average site-specific r-WGS TOFs for 10 and 0.25 $CO_2:H_2$ ratios were 0.029 and 0.0049 CO molecules/Rh_{iso} site/s, respectively. The same analysis and similar linear trends were observed for the methanation rate and Rh_{NP} sites, which yielded average site-specific methanation TOF for 10 and 0.25 $CO_2:H_2$ of 0.0059 and 0.024 CH_4 molecules/Rh_{NP} site/s, respectively. While we expect the site-specific TOF for r-WGS on Rh_{iso} sites to be relatively constant for all Rh_{iso} sites, the site-specific methanation TOFs on Rh_{NP} sites represent the population weighted average of the TOF specific to various site types (terrace, edge, and corner) that exist on metal nanoparticle surfaces. This last point is discussed more thoroughly in the Discussion. As mentioned earlier, throughout the remainder of the paper we will explicitly state
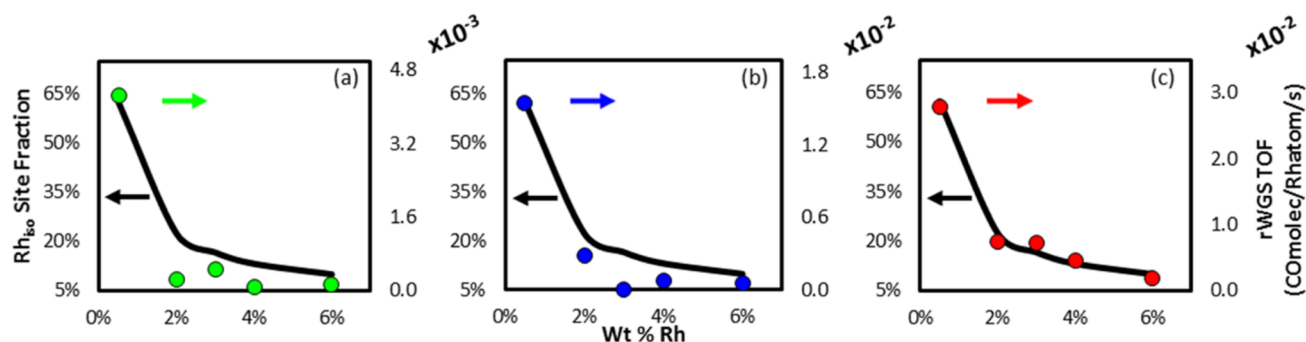
Figure 3. Rh_{iso} site fraction and r-WGS TOF plotted as a function of wt % Rh at (a) $1CO_2{:}4H_2$, (b) $3CO_2{:}H_2$, and (c) $10CO_2{:}H_2$ feed ratios. The left axes are Rh_{iso} site fractions, which are displayed in the plots as a black line connecting the measured values for graphical clarity. The green, blue, and red data points correspond to measured r-WGS TOF and are quantified in the right axis of each plot.
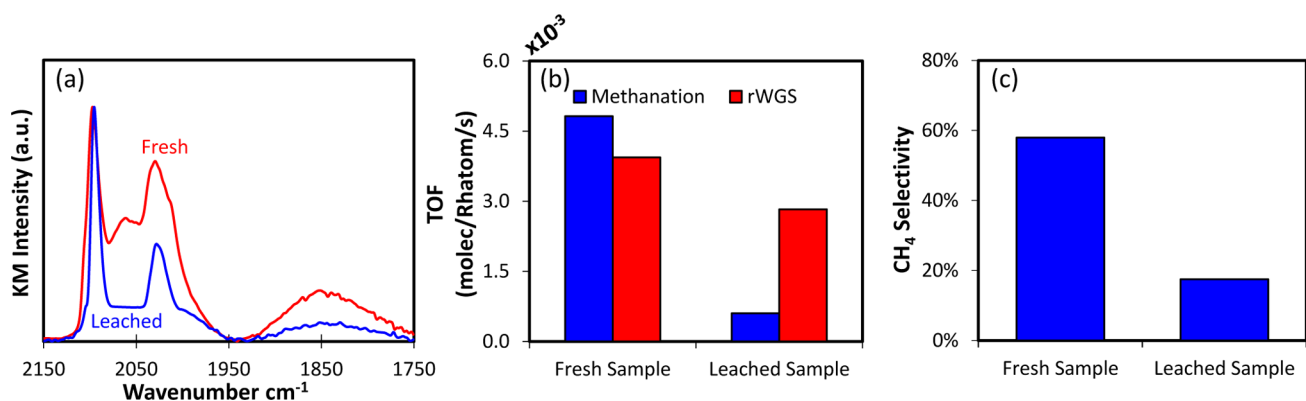
Figure 4. (a) DRIFT spectra for CO adsorbed on the fresh 2% Rh/TiO_2 and HCl/H_2O_2 leached samples, where spectra are displayed in KM units and normalized by the symmetric *gem*-dicarbonyl peak (2097 cm^{-1}) height. (b) TOF for both CO_2 reduction pathways measured on the fresh 2% Rh/TiO_2 and leached samples at 200 °C and a feed ratio of $3CO_2{:}H_2$. The quantified number of Rh sites for the fresh catalyst was also used for the TOF calculations in the leached sample; see main text for discussion on this. (c) CH_4 selectivity plotted for the fresh and leached samples at 200 °C and a feed ratio of $3CO_2{:}H_2$.

when we are discussing site-specific TOFs, which refer to the TOFs for a specific reaction on the basis of specific site type concentration (Rh_{iso} or Rh_{NP}). Otherwise, the reported TOFs will be on the basis of reaction rates per total number of sites (Rh_{iso} + Rh_{NP}).

The agreement in the trends between the site fraction and TOF in Figure 3 and Supporting Information Figure S6 and the linearity displayed in Supporting Information Figure S7 suggest that the relative fraction of Rh_{iso} sites controls the TOF for CO production, whereas the relative fraction of Rh_{NP} sites controls the TOF for CH_4 production. Thus, selectivity between the branching pathways of CO_2 reduction into CO and CH_4 is controlled by the ratio of these site types. This selectivity controlling mechanism is further substantiated by incongruence between the relatively constant particle sizes and large variations in TOF values in the Rh weight loading range 0.5−4%, suggesting that particle size effects do not significantly control the observed variations in selectivity.

3.2. Impact of Nanoparticle Leaching. Quantitative agreement between variations in the TOFs and site fractions as a function of Rh weight % allowed us to postulate that the Rh_{iso} and Rh_{NP} sites operate as nearly exclusive active sites for driving their respective CO and CH_4 production reaction pathways. Another simple approach to probe the reactivity of a particular site type is to test the selectivity of a material with one exclusive site type. Leaching has been previously used to distinguish the importance of isolated catalytic sites from nanoparticle-based

sites, by removing the nanoparticles and observing very little change in the catalytic activity, suggesting the nanoparticles served more as a spectator than active catalyst site. For example, NaCN-based leaching has been used to remove Au clusters and nanoparticles from a support without leaching away the single Au sites to identify the single Au sites as being the active site for driving the WGS reaction.[10,11] In a similar thought process, we treated a 2% Rh/TiO_2 sample with a HCl/H_2O_2-based leaching process to remove Rh_{NP} sites from the support and substantiate the relationship between Rh_{iso}/Rh_{NP} site fraction and CO_2 reduction selectivity.[21] Figure 4a shows DRIFT spectra for CO chemisorbed to the 2% Rh catalyst before and after leaching. A significant decrease in the relative fraction of Rh_{NP} sites (from 78% to 51%) was observed, as indicated by the significant decrease in the CO-linear and CO-bridge peak intensities (2068 and 1860 cm^{-1}). Although the nanoparticles were not completely removed, the significant change in the site fraction suggests that the leaching procedure selectively removed Rh nanoparticles, leaving behind a majority of Rh_{iso} sites on the support. Because volumetric CO chemisorption experiments were not executed after leaching, the DRIFT spectra only allow us to assert that the relative fraction of Rh_{NP} sites decreased significantly, but we cannot comment on the absolute number of each site type remaining.

Catalytic testing of the leached material at $3CO_2{:}H_2$ conditions and 200 °C showed a significant reduction in the CH_4 production TOF (−88%), with a decrease in r-WGS TOF

to a much lesser degree (−28%) as compared to the same experiment performed on fresh material, Figure 4b. The reported TOFs for the leached material were calculated using the fresh material's surface area (Rh sites/weight), and as a result the change in TOFs is representative of the absolute changes in the number of each site type due to leaching, suggesting a fairly complete leaching of Rh nanoparticles from the support. The larger decrease in CH_4 production TOF, as compared to CO production TOF, as a result of leaching led to a decrease in CH_4 selectivity from 58% to 17%, Figure 4c. The leaching-induced decrease in CH_4 selectivity of ∼40% is reasonably consistent with the measured decrease in Rh_{NP} site fraction of ∼27%, particularly when considering other potential impacts of the leaching procedure including Cl poisoning of nanoparticle sites. The correlated relationships between Rh_{iso} (Rh_{NP}) site concentration and CO (CH_4) production (analyzed by Rh wt % dependence and leaching) provide strong evidence that Rh_{iso} sites are highly selective for CO production, whereas Rh_{NP} sites are highly selective for CH_4 production.

3.3. Site Switching Controls Instability. At the most H_2-lean conditions, $10CO_2$:H_2, the agreement between weight loading-dependent trends for the CO (CH_4) TOF and Rh_{iso} (Rh_{NP}) site fractions was not as good as under more H_2-rich conditions (see Supporting Information Figure S6). Examination of time-dependent changes in catalytic reactivity provides evidence explaining this behavior and further substantiates the assigned site type−reactivity relationships. The deviation in agreement observed for the $10CO_2$:H_2 feed ratio is due to an observed change in the reactivity of the catalyst under these conditions during the course of the TOF measurement; TOFs were calculated on the basis of the average measured rate in the first hour under reaction conditions. Figure 5a and b shows the rates of change of the measured TOFs ((dTOF)/(dt)) for CO and CH_4 production at CO_2:$4H_2$ and $10CO_2$:H_2 feed conditions, respectively, calculated for the first hour under reaction conditions (see Supporting Information Figure S8 for an explanation of the rate of change calculation). Figure 5a shows that all tested catalysts were stable under CO_2:$4H_2$ reaction conditions for the first hour on stream. However, under $10CO_2$:H_2 feed conditions, the CO TOF increased with time on stream, while the CH_4 TOF decreased with time on stream. There was a quantitative agreement between the rates of TOF change for CO and CH_4 production, respectively, at all Rh weight loadings. These results, combined with the site type−reactivity relationships assigned above, suggest that under H_2-lean reaction conditions Rh nanoparticles disintegrate to form increased concentrations of Rh_{iso} sites and that this process controls the increase in CO TOF and concomitant decrease in CH_4 TOF with time on stream. The changing reactivity during the first hour on stream at the $10CO_2$:H_2 feed conditions also explains why the trends in TOF and site concentration seen in Supporting Information Figure S6 are not in excellent agreement, because the fraction of site types was changing during the TOF measurements.

To quantitatively explore the proposed reaction condition-induced Rh nanoparticle disintegration mechanism, CO chemisorption DRIFTS measurements were used to determine the fraction of Rh_{iso} and Rh_{NP} sites before and after 90 min on stream under $10CO_2$:H_2 feed ratio and 200 °C; see section 2.3.3 for details. Figure 6a shows an example of data obtained from these measurements, where DRIFT spectra for CO adsorbed at 300 K and saturation coverage before and after 90 min on stream are compared for a 6% Rh/TiO_2 sample. The
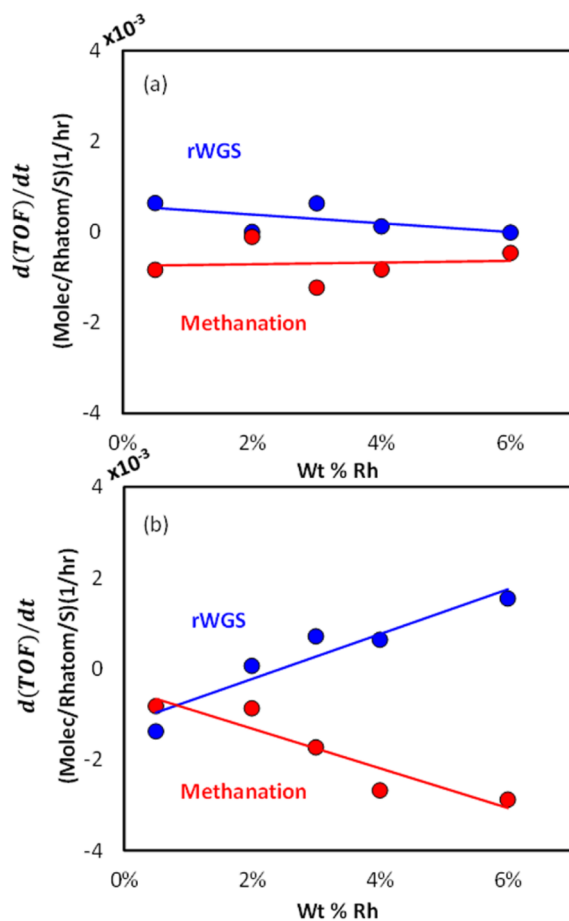
Figure 5. Rate of TOF change (d(TOF)/dt) for both reaction pathways as a function of wt % Rh measured at 200 °C and feed ratio of (a) $0.25CO_2$:H_2 and (b) $10CO_2$:H_2. Rates of change for the r-WGS TOF are shown in blue points and methanation TOF in red points. The linear fits to the data are added for visual clarity.

relative strength of the peaks associated with the Rh_{NP} sites slightly decreases due to reaction conditions. Alternatively, the relative strength of the peaks associated with Rh_{iso} sites increased significantly after 90 min on stream. This suggests that under reaction conditions, metal atoms from Rh nanoparticles disperse to form isolated Rh atoms on TiO_2. Although the spectra taken after the reaction looks to have had a net increase in total sites, this can be explained by the much larger extinction coefficient corresponding to the Rh_{iso} sites than the Rh_{NP} sites. As previously mentioned, the bridge peak resolution may have limited our ability to observe a change in intensity due to time-on-stream. Once again, the CO chemisorption DRIFT spectra are only used to calculate relative Rh_{NP} and Rh_{iso} site fractions, but not to quantify the absolute number of sites. To calculate a change in relative site fractions due to reaction conditions, it was assumed that the loss of Rh_{NP} sites was due exclusively to a gain in Rh_{iso} sites; no Rh vaporization or dissolution into the TiO_2 bulk were considered. These measurements were performed for all five Rh weight loadings.

The measured rates of change in CH_4 selectivity and fraction of Rh_{NP} sites are shown in Figure 6b and c, respectively, as a function of Rh weight loading. At the lowest Rh weight loading (0.5%), a 4% decrease in the CH_4 selectivity and 3% reduction in the fraction of Rh_{NP} sites were observed for the first hour on
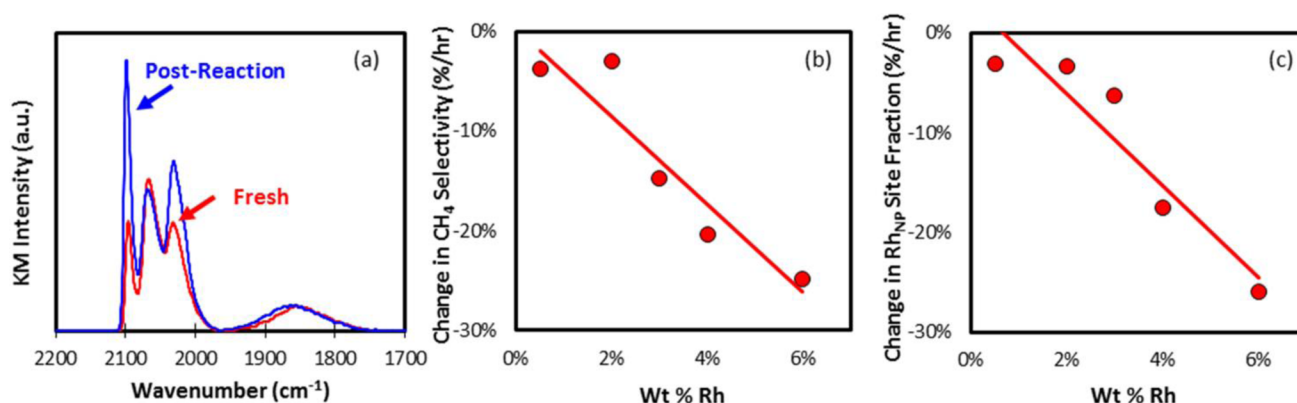
Figure 6. (a) DRIFT spectra of CO adsorbed at 300 K on the fresh 6 wt % Rh/TiO_2 sample and after 90 min under reaction conditions at 200 °C and $10CO_2:H_2$ feed ratio. The spectra are presented in baseline subtracted, raw KM units with no normalization. (b) Rate of CH_4 selectivity change (%/h) measured at conditions identical to those in (a). (c) Rate of Rh_{NP} site loss (%/h), resulting in Rh_{iso} site production, measured at conditions identical to those in (a) and (b).

stream. However, the 6% Rh sample showed a 27% decrease in CH_4 selectivity and 26% reduction in fraction of Rh_{NP} sites during the first hour on stream. Figure 6b and c shows an excellent correlation between the change in CH_4 selectivity and the conversion of Rh_{NP} sites into Rh_{iso} sites as a function of time on stream for all Rh weight loadings. Furthermore, it was observed that the rate of loss in methane selectivity and Rh_{NP} site fraction increased with increasing Rh weight loading. The results shown in Figures 5 and 6 provide strong evidence that the observed reduction in CH_4 selectivity with time on stream in H_2-lean conditions is due to reaction condition-induced disintegration of Rh nanoparticles to form a higher concentration of Rh_{iso} sites that are uniquely selective for CO production. On the basis of the higher rate of selectivity and site fraction change at higher Rh weight loadings, it also seems that the driving force for the reaction condition-induced disintegration of Rh nanoparticles is the initial concentration of Rh nanoparticles.

4. DISCUSSION

Recent reports have demonstrated the significant catalytic reactivity of supported isolated catalytic atoms or single atoms that were previously masked by the coexistence of metal clusters or nanoparticles. A majority of this work investigated noble metals (Pt, Pd, Au, and Rh) catalyzing the water–gas-shift (WGS) reaction and CO oxidation.[7,10−12,29−33] For instance, Fu et al. identified the water–gas-shift active site to be single nonmetallic Au or Pt atoms supported on ceria, where the metallic nanoparticles served as spectator species.[10] Another interesting application of isolated catalytic atoms is the single atom alloy system, where a metal is isolated at the surface of a different metal to exploit the functionality of both metals. Kyriakou et al. showed that functionality can be added by introducing isolated Pd atoms, which drive H_2 dissociation on a Cu surface that allows for facile product desorption, to obtain a more ideal balance between dissociation and desorption.[7] These reports typically rely on synthetic protocols to create catalysts with a predominance of single isolated sites and microscopy- or spectroscopy-based characterizations to identify the existence of the species. Through this approach reactivity assignments of the isolated sites are demonstrated. However, in these approaches it can be difficult to quantitatively demonstrate these relationships due to the small sample size of microscopy-based characterization, or

difficult fitting procedures for X-ray absorption spectroscopy analysis of samples with heterogeneous distributions of metal cluster sizes.[34] Furthermore, the focus of these studies has been on the unique reactivity of isolated sites in single reaction pathway reactions (i.e., only one potential product) rather than the potential for isolated sites to exhibit unique selectivity as compared to nanoparticles consisting of the same metal.

Unlike the previous demonstrations, our investigation relies on site-specific characterization approaches that allow for quantitative site type−reactivity assignments, which demonstrate that isolated metal atoms and metal nanoparticles composed of the same metal on the same support can exhibit unique selectivity in a parallel reaction pathway. Similar relationships were recently suggested for Pd- and Ru-based systems, although only qualitative evidence could be provided based on TEM analyses of the catalysts.[19,20] In addition, unique reactivity of $Rh(C_2H_4)_2$ complexes and few atom Rh clusters for ethane hydrogenation and dimerization have been qualitatively correlated on the basis of X-ray absorption spectroscopy.[12] In our studies, the DRIFTS-based CO chemisorption characterization approach was crucial for quantifying site type fractions and allowing proper CO:Rh normalization of total Rh site concentrations that enabled quantitative TOF calculations. In demonstrating quantitative site type−reactivity relationships, we relied on the unique frequencies and existing extinction coefficients for CO intramolecular vibrational modes on different Rh site types. In the context of single site reactivity, our work highlights the utility of probe molecule FTIR spectroscopy for quantifying the concentration of isolated and nanoparticle metal sites on a catalyst to convincingly assign the unique reactivity to each site type in parallel reaction pathways.

It is worth discussing a quantitative comparison of the results shown in Supporting Information Figure S7, and Figures 5b and 6b,c. The measurements in Supporting Information Figure S7 show that at a $10CO_2:H_2$ feed ratio the average site-specific r-WGS TOF on Rh_{iso} sites is 0.029 molecules CO/Rh_{iso} site/s, while the site-specific methanation TOF on Rh_{NP} sites was determined to be 0.0059 molecules CH_4/Rh_{NP} site/s. This shows that the site-specific TOF for the r-WGS reaction on the Rh_{iso} sites is nearly 5 times faster than the average site-specific methanation TOF on the Rh_{NP} sites at these conditions. However, under the same conditions, there is a proportional 1:1 agreement observed between the rates of change in TOF

(d(TOF)/dt) for the r-WGS (increase) and methanation (decrease), as shown in Figure 5b. Consistent with the data in Figure 5b, there is also a 1:1 agreement between the decrease in methane selectivity and in Rh_{NP} site fraction, as shown in Figure 6b and c. The proportional agreement observed in Figures 5 and 6 requires the following equality to hold true:

$$TOF_{iso} \times \Delta Rh_{iso} = \sum_{i=1}^{n} TOF_{NP,i} \times \Delta Rh_{NP,i}$$

In this equality, the TOFs represent site-specific TOFs, where TOF_{iso} is for r-WGS on Rh_{iso} sites and TOF_{NP} are for methanation on Rh_{NP} sites. On the basis of the results in Figure 3, and Supporting Information Figures S6 and S7, it is assumed that r-WGS only occurs at Rh_{iso} sites, while methanation only occurs at Rh_{NP} sites. The ΔRh's represent the change in concentration of each site type due to time on stream under reaction conditions, which we attribute primarily to the disintegration of nanoparticles to form Rh_{iso} sites. For Rh_{NP} sites, a concentration-weighted sum is used because different sites existing on nanoparticles (corner, edge, terrace, and perimeter) potentially exhibit different site-specific methanation TOFs. To rationalize this equality in the context of the measured average site-specific TOF, we will first consider how the disintegration of nanoparticles to form isolated sites occurs.

Recently, it was predicted that smaller Rh particles are more likely to undergo disintegration than larger Rh particles, due to their high surface free energies.[35,36] The small particles (<1.5 nm) that are most likely to disintegrate have high surface to bulk atom ratios (dispersions nearing 1), and thus when a single Rh_{NP} atom is removed from a small nanoparticle to form an Rh_{iso} site on the support, it is likely that there would not be an underlying bulk Rh atom to expose. This suggests that $\Delta Rh_{iso} \approx \sum_{i=1}^{n} \Delta Rh_{NP,i}$. Considering the similar absolute change in Rh_{iso} and Rh_{NP} site concentrations and the average site-specific TOF ratio of ~5TOF_{iso}:TOF_{NP} under conditions explored in Figures 5 and 6, the Rh_{NP} sites that transfer from the nanoparticle surface to become Rh_{iso} sites must have site-specific methanation TOFs much larger than the average site-specific methanation TOF_{NP}. The proposed difference in reactivity between different site types is justified by recent studies showing that the CO_2 methanation TOF on Ru nanoparticles increases ~5-fold in the diameter window 1−1.5 nm.[37] On the basis of this analysis, we propose that the change in CH_4 selectivity with time on stream occurs by disintegration of small Rh nanoparticles to form Rh_{iso} sites and that disintegration occurs by loss of Rh_{NP} sites that exhibit site-specific methanation TOF much larger than the average site-specific TOF of all Rh_{NP} sites. Future studies will focus on exploring this disintegration process, specifically to identify the nanoparticle sizes that are most probable to disintegrate and on the types and number of Rh_{NP} sites being lost during this process.

Our results raise questions about why the two active site types (Rh_{NP} and Rh_{iso}) exhibit such different selectivity in CO_2 reduction. The significant difference in CO_2 reduction selectivity can be rationalized by considering the ensemble of active sites surrounding Rh_{iso} and Rh_{NP} sites. Rh sites located on a nanoparticle, Rh_{NP}, will be surrounded by other Rh sites that are active for H_2 dissociation, but also bind CO very strongly. This suggests that sequential steps hydrogenating CO, or directly CO_2, to produce CH_4 will be favored over CO desorption.[38,39] Alternatively, isolated Rh sites on oxide supports bind CO more weakly than Rh nanoparticles sites, suggesting that the final step for r-WGS should be more facile on Rh_{iso} sites as compared to Rh_{NP} sites. In addition, the lack of atomic H adsorption sites on the oxide support surrounding Rh_{iso} sites suggests that sequential hydrogenations of CO or CO_2 on the oxide or Rh_{iso} site would be quite improbable. Another way the selectivity difference between the Rh_{NP} and Rh_{iso} can be rationalized is based on the difficulty associated with an 8-electron reduction of CO_2 to CH_4 occurring at single metal atoms, which would be more facile at an Rh_{NP} site with an ensemble of other Rh atoms surrounding. This simple mechanistic picture substantiates our proposed assignments of Rh_{iso} sites being uniquely active for r-WGS and Rh_{NP} sites being uniquely active for CO_2 methanation.

It is also important to discuss the observed reaction condition-induced disintegration of Rh nanoparticles into Rh_{iso} sites that is in opposition to typically seen agglomeration of small collections of metal atoms into larger nanoparticles, Ostwald ripening. Previous studies have shown that exposure of Rh nanoparticles on oxide supports to ambient temperature CO environments induced disintegration of nanoparticles into isolated Rh sites.[8,27,35,40] It has also been shown that elevated temperatures, in solely H_2 or CO environments, can cause the Rh_{iso} sites to reassociate with nearby Rh nanoparticles.[27,41] To investigate the effect of reaction environment on disintegration, we tested 6% Rh/TiO_2 at 200 °C in 10% CO_2:1% H_2, 10% CO_2, 10% CO:4% H_2, and 10% CO all with an Ar balance for 90 min. 10% CO_2 had no observable effect on site fractions, whereas both 10% CO:4% H_2 and 10% CO caused the Rh_{iso} sites to convert to Rh_{NP} sites in direct contrast to the Rh_{NP} to Rh_{iso} conversion observed at 10% CO_2:H_2 shown in Figure 6. The results suggest that high chemical potentials of surface bound species specific to CO_2 methanation on Rh nanoparticles experienced under the H_2-lean conditions (10CO_2:H_2) drove the disintegration of Rh nanoparticles into Rh_{iso} sites. Furthermore, the driving force for the disintegration may be a complex function of surface bound species on Rh, as well as the TiO_2 surface termination, which could both impact the stability of isolated sites.

5. CONCLUSIONS

To summarize, we have demonstrated quantitative relationships between the concentration of isolated and nanoparticle-based Rh sites on TiO_2 supports and the CO_2 reduction selectivity toward CO and CH_4 production, respectively. It was also observed that the relative fraction of these site types on TiO_2 changes dynamically under reaction conditions through nanoparticle disintegration to form isolated sites and that this process controls the unstable reactivity of higher Rh weight loadings under H_2-lean conditions with time on stream. These insights provide important information for the design of highly reactive and selective CO_2 reduction catalysts and stress the importance of considering how the catalyst structures may change under reaction conditions. Furthermore, this work emphasizes the importance of considering catalytic sites that may go undetected with traditional TEM approaches when developing rigorous structure function relationships in catalysis.

■ ASSOCIATED CONTENT

ⓢ Supporting Information

Full experimental details and supporting figures. This material is available free of charge via the Internet at http://pubs.acs.org.

AUTHOR INFORMATION

Corresponding Author
*christopher@engr.ucr.edu

Notes
The authors declare no competing financial interest.

ACKNOWLEDGMENTS

REFERENCES

(1) Nørskov, J. K.; Bligaard, T.; Hvolbaek, B.; Abild-Pedersen, F.; Chorkendorff, I.; Christensen, C. H. *Chem. Soc. Rev.* **2008**, *37*, 2163.

(2) Schweitzer, N. M.; Schaidle, J. a.; Ezekoye, O. K.; Pan, X.; Linic, S.; Thompson, L. T. *J. Am. Chem. Soc.* **2011**, *133*, 2378.

(3) Christopher, P.; Linic, S. *J. Am. Chem. Soc.* **2008**, 11264.

(4) Christopher, P.; Linic, S. *ChemCatChem* **2010**, *2*, 78.

(5) Andersson, M. P.; Abild-Pedersen, F.; Remediakis, I. N.; Bligaard, T.; Jones, G.; Engbaek, J.; Lytken, O.; Horch, S.; Nielsen, J. H.; Sehested, J.; Rostrup-Nielsen, J. R.; Chorkendorff, I. *J. Catal.* **2008**, *255*, 6.

(6) Underwood, R. P.; Bell, A. T. *Appl. Catal.* **1987**, *34*, 289.

(7) Kyriakou, G.; Boucher, M. B.; Jewell, A. D.; Lewis, E. a.; Lawton, T. J.; Baber, A. E.; Tierney, H. L.; Flytzani-Stephanopoulos, M.; Sykes, E. C. H. *Science* **2012**, *335*, 1209.

(8) Tao, F.; Dag, S.; Wang, L.-W.; Liu, Z.; Butcher, D. R.; Bluhm, H.; Salmeron, M.; Somorjai, G. a. *Science* **2010**, *327*, 850.

(9) Tao, F.; Grass, M. E.; Zhang, Y.; Butcher, D. R.; Renzas, J. R.; Liu, Z.; Chung, J. Y.; Mun, B. S.; Salmeron, M.; Somorjai, G. A. *Science* **2008**, 932.

(10) Fu, Q.; Saltsburg, H.; Flytzani-Stephanopoulos, M. *Science* **2003**, *301*, 935.

(11) Flytzani-Stephanopoulos, M. *Acc. Chem. Res.* **2014**, *47*, 783.

(12) Serna, P.; Gates, B. C. *J. Am. Chem. Soc.* **2011**, *133*, 4714.

(13) Peterson, E. J.; DeLaRiva, A. T.; Lin, S.; Johnson, R. S.; Guo, H.; Miller, J. T.; Kwak, J. H.; Peden, C. H. F.; Kiefer, B.; Allard, L. F.; Ribeiro, F. H.; Datye, A. K. *Nat. Commun.* **2014**, *5*, 4885.

(14) Karelovic, A.; Ruiz, P. *J. Catal.* **2013**, *301*, 141.

(15) González-Carballo, J. M.; Pérez-Alonso, F. J.; Ojeda, M.; García-García, F. J.; Fierro, J. L. G.; Rojas, S. *ChemCatChem* **2014**, *6*, 2084.

(16) Bezemer, G. L.; Bitter, J. H.; Kuipers, H. P. C. E.; Oosterbeek, H.; Holewijn, J. E.; Xu, X.; Kapteijn, F.; van Dillen, A. J.; de Jong, K. P. *J. Am. Chem. Soc.* **2006**, *128*, 3956.

(17) Behrens, M.; Studt, F.; Kasatkin, I.; Kühl, S.; Hävecker, M.; Abild-Pedersen, F.; Zander, S.; Girgsdies, F.; Kurr, P.; Kniep, B.-L.; Tovar, M.; Fischer, R. W.; Nørskov, J. K.; Schlögl, R. *Science* **2012**, *336*, 893.

(18) Karelovic, A.; Ruiz, P. *Appl. Catal., B: Environ.* **2012**, *113–114*, 237.

(19) Kwak, J. H.; Kovarik, L.; Szanyi, J. *ACS Catal.* **2013**, *3*, 2449.

(20) Kwak, J. H.; Kovarik, L.; Szanyi, J. *ACS Catal.* **2013**, *3*, 2094.

(21) Harjanto, S.; Cao, Y.; Shibayama, A.; Naitoh, I.; Nanami, T.; Kasahara, K.; Okumura, Y.; Liu, K.; Fujita, T. *Mater. Trans.* **2006**, *47*, 129.

(22) Sirita, J.; Phanichphant, S.; Meunier, F. C. *Anal. Chem.* **2007**, *79*, 3912.

(23) Duncan, T. M.; Yates, J. T., Jr.; Vaughan, R. W. *J. Chem. Phys.* **1980**, *73*, 975.

(24) Yang, A. C.; Garland, C. W. *J. Phys. Chem.* **1957**, *61*, 1504.

(25) Yates, J. T., Jr.; Duncan, T. M.; Worley, S. D.; Vaughan, R. W. *J. Chem. Phys.* **1979**, *70*, 1219.

(26) Cavanagh, R. R.; Yates, J. T., Jr. *J. Chem. Phys.* **1981**, *74*, 4150.

(27) Solymosi, F.; Pásztor, M. *J. Phys. Chem.* **1985**, 4789.

(28) Zhang, Z.; Verykios, X. *J. Catal.* **1994**, *148*, 737.

(29) Boccuzzi, F.; Chiorino, A.; Manzoli, M.; Andreeva, D.; Tabakova, T. *J. Catal.* **1999**, *185*, 176.

(30) Fu, Q.; Deng, W.; Saltsburg, H.; Flytzani-Stephanopoulos, M. *Appl. Catal., B: Environ.* **2005**, *56*, 57.

(31) Fu, Q.; Kudriavtseva, S.; Saltsburg, H.; Flytzani-Stephanopoulos, M. *Chem. Eng. J.* **2003**, *93*, 41.

(32) Liu, Z.-P.; Jenkins, S.; King, D. *Phys. Rev. Lett.* **2005**, *94*, 196102.

(33) Yang, M.; Allard, L. F.; Flytzani-Stephanopoulos, M. *J. Am. Chem. Soc.* **2013**, *135*, 3768.

(34) Fierro-Gonzalez, J. C.; Kuba, S.; Hao, Y.; Gates, B. C. *J. Phys. Chem. B* **2006**, *110*, 13326.

(35) Goldsmith, B. R.; Sanderson, E. D.; Ouyang, R.; Li, W.-X. *J. Phys. Chem. C* **2014**, *118*, 9588.

(36) Ouyang, R.; Liu, J.-X.; Li, W.-X. *J. Am. Chem. Soc.* **2013**, *135*, 1760.

(37) Abdel-Mageed, A. M.; Eckle, S.; Anfang, H. G.; Behm, R. J. *J. Catal.* **2013**, *298*, 148.

(38) Beuls, A.; Swalus, C.; Jacquemin, M.; Heyen, G.; Karelovic, A.; Ruiz, P. *Appl. Catal., B: Environ.* **2012**, *113–114*, 2.

(39) Porosoff, M. D.; Chen, J. G. *J. Catal.* **2013**, *301*, 30.

(40) Kruse, N.; Gaussmann, A. *J. Catal.* **1993**, *144*, 525.

(41) Solymosi, F.; Pásztor, M. *J. Phys. Chem.* **1986**, *90*, 5312.